Real Time Polarization Light Curves for Space Debris and Satellites

Dr. John Stryjewski
Dan Hand,
CSC-ISTEF
Dr. David Tyler
Sukumar Murali
College of Optics, University of Arizona
Dr. Mike Roggemann
Nick Peterson
Department of Electric and Computer Engineering
Michigan Technological University

09/17/2010

Abstract

In recent years there as been a lot of interest in using the time history of reflected solar light (light curves) from satellites and space debris as a means of determining shape and material composition. Most of these studies used time series analysis in an attempt to classify objects while some have used multi-spectral or spectroscopic approaches. One of the difficulties that most of these approaches had was the lack of high fidelity shape and material modeling. Here we present a high fidelity modeling approach that correctly describes the shape, material and dynamics of space objects. Furthermore, this model, in real time, correctly models reflection, emission, glint and polarization effects. We use this model to show how detection of polarization effects can help characterize both satellites and space debris. Polarization approaches have an advantage over spectroscopic or intensity based method because polarization is unaffected by the atmosphere. We present a comparison of polarization approaches for the analysis of space debris and satellites and discuss the advantages of being able to do these calculations in real time.

Introduction

The time variation of reflected sunlight from a satellite or space debris is referred as a "light curve". Light curves have been used for many years [15, 20, 13, 14, 18, 19]to characterize both satellites and space debris. Most of these investigations attempt to deduce satellite material and orientation by measuring the total reflected intensity of the sunlight measured as a function of the solar-observer angle. One of the main limitations of these approaches is that without some a priori knowledge of the space object's shape, it is difficult to draw any conclusions about the orientation. Some studies attempted to determine material properties from multi-spectral observation of light curves. These studies were also inconclusive because satellites and debris are rarely composed of a single material. What is need is an approach that can measure material propertied *independent* from shape. If that is possible, then it is likely that orientation and can be inferred from changes in the material composition as viewing aspect changes. Once material composition and orientation are known then shape determination may be possible.

In this paper we present one possible approach to determining, simultaneously, the material composition (and surface finish), orientation and shape of satellites and space debris. Our approach relies on measurements of the polarization of the reflected sunlight (polarization light curves) and on a sophisticated real-time, dynamic model of satellites and space debris. As we will show in this paper, the polarization signature for a space object provides a shape independent measure of material composition. The high fidelity dynamic, polarized, light scattering model we use here is based on the approach we presented at the 2009 AMOSTECH Conference[16]. The model presented in the 2009 paper was designed to study polarization effects for active (laser) illumination of LEO satellites. For this paper we have extended the model to also include the effects of solar illumination.

In addition to the presentation of the high resolution model. we will investigate the efficacy of using polarization light curves to determine satellite or space debris properties using simulations. Lastly, we will discuss the utility of this approach to several real time applications including: space object ID verifications, satellite aging and health studies, and real time pose estimation.

Polarization Signatures

When light is scattered from a surface a flat (specular) surface, the intensity of the reflected light depends on only the index of refraction of the material and is given by the Fresnel Equations[1]:

---

[1]These equations assume the light is incident from vacuum

$$r_s = \frac{\sqrt{n^2 - sin(\theta)^2} - cos(\theta)}{\sqrt{n^2 - sin(\theta)^2} + cos(\theta)} \tag{1}$$

$$r_p = \frac{n^2 cos(\theta) - \sqrt{n^2 - sin(\theta)^2}}{n^2 cos(\theta) + \sqrt{n^2 - sin(\theta)^2}} \tag{2}$$

Here, n is the index of refraction of the material, r_s and r_p are the reflection coefficients for the S and P polarization Fields respectively and θ is the angle the incident ray makes with the normal. For dielectrics the transmission through the surface is simply $1 - r$. For metals (more than a few wavelengths in thickness) there is no transmission but there is absorption. This absorption is usually taken into account by making the index of refraction complex.

$$n_{metal} = n + ik \tag{3}$$

Figure 1 show the Fresnel coefficients for gold and BK7 (glass). The middle subplots show the intensity
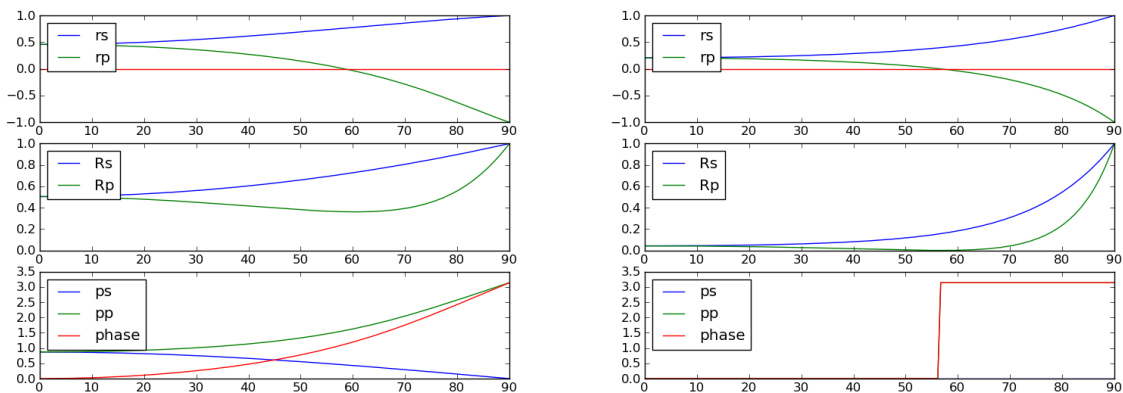

Figure 1: The Fresnel reflection coefficients for gold (left) and for bk7 glass (right). The top subplot is the field coefficients, the middle is the intensity coefficients and the bottom is the phase delay (red line is the relative phase delay).

reflection coefficients or reflectivities for the S and P polarizations. The graphs on the left are for gold at 0.5micons and the graphs on the right are for BK7 glass. Two features are important to note. First, for bk7, a dielectric, the S-polarization is completely attenuated when the incident angle is approximately 57°; This is the well known Brewster angle. Second, above 25° incident angle there is a significant difference between the S and P reflectivities for both gold (conductor) and BK7 (dielectric). This last point is important because, in solar scattering from Low Earth Orbit (LEO) Satellites , the incident angles are generally greater than 20° and we would therefore expect a strong polarization signature. For high orbits (geosynchronous) the solar incident angles will still be larger than 20° for most of the orbit. For the rest of this paper we will discuss scattering in terms of the total angle between incident and reflected rays, or twice the incident angle (see Figure 2).

For partially polarized or unpolarized light, it is best to describe scattering not in terms of the incident and reflected S and P polarizations but, in terms of the Stokes parameters:

$$
\begin{aligned}
I &= S_0 = E_s E_s^* + E_p E_p^* \\
Q &= S_1 = E_s E_s^* + E_p E_p^* \\
U &= S_2 = 2Re(E_s E_p^*) \\
V &= S_3 = 2Re(E_s E_p^*)
\end{aligned}
\tag{4}
$$

Where E is the electric field and the S and P subscripts refer to the S and P polarizations. In this notation the Degree of Polarization (DOP) of the light is defined as:

$$DOP = \frac{Q^2 + U^2 + V^2}{I^2} \tag{5}$$

Figure 2: The phase angle (θ), the angle between the sun and the observer.

Since sunlight is unpolarized, the incident light on the space object is described by the Stokes parameters $I \geq 0, Q = U = V = 0$. or equivalently by the Stoked Vector:

$$\overrightarrow{S} = \begin{bmatrix} I \\ Q \\ U \\ V \end{bmatrix} = \begin{bmatrix} I \\ 0 \\ 0 \\ 0 \end{bmatrix} \tag{6}$$
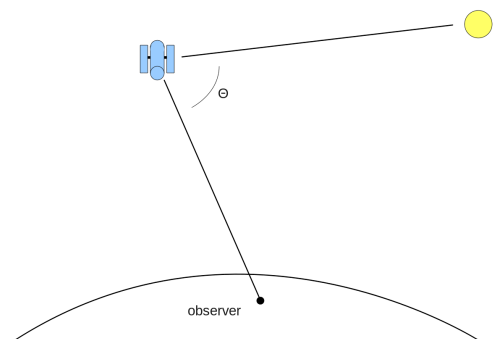
After reflection from from the satellite, the Stokes vector will, in general, be

$$
\overrightarrow{S} = \begin{bmatrix} I' \\ Q' \\ U' \\ V' \end{bmatrix} = \begin{bmatrix} I' < I \\ Q' \neq 0 \\ U' \neq 0 \\ V' \neq 0 \end{bmatrix}
\tag{7}
$$

For scattering that exhibits polarization effects, the reflection may be described by the Mueller matrix8:

$$
\begin{bmatrix} S'_0 \\ S'_1 \\ S'_2 \\ S'_3 \end{bmatrix} = \begin{bmatrix} M_{00} & M_{01} & M_{02} & M_{03} \\ M_{10} & M_{11} & M_{12} & M_{13} \\ M_{20} & M_{21} & M_{22} & M_{23} \\ M_{30} & M_{31} & M_{32} & M_{33} \end{bmatrix} \cdot \begin{bmatrix} S_0 \\ S_1 \\ S_2 \\ S_3 \end{bmatrix}
\tag{8}
$$

Where S' is the stokes vector which describes the polarization state of the reflected light. While the Mueller matrix can be used to describe the change in polarization when light reflects from a uniform, flat surface, it is not restricted to describing specular reflections and in general is a function of both incident light angle and output light angle. Furthermore if the material is anisotropic, the Mueller matrix will also depend on material orientation.

For the special case of unpolarized incident light however, the only matrix elements that are important are:

$$
\begin{bmatrix} S'_0 \\ S'_1 \\ S'_2 \\ S'_3 \end{bmatrix} = \begin{bmatrix} M_{00} & 0 & 0 & 0 \\ M_{10} & 0 & 0 & 0 \\ M_{20} & 0 & 0 & 0 \\ M_{30} & 0 & 0 & 0 \end{bmatrix} \cdot \begin{bmatrix} S_0 \\ 0 \\ 0 \\ 0 \end{bmatrix}
\tag{9}
$$

The elements:

$$
\begin{bmatrix} M_{10} \\ M_{20} \\ M_{30} \end{bmatrix}
\tag{10}
$$

are referred to as the polarizance. The Mueller matrix approach makes no assumption about the underlying scattering mechanism and if we are to calculate it from theory we must use a microscopic description of surface scattering.
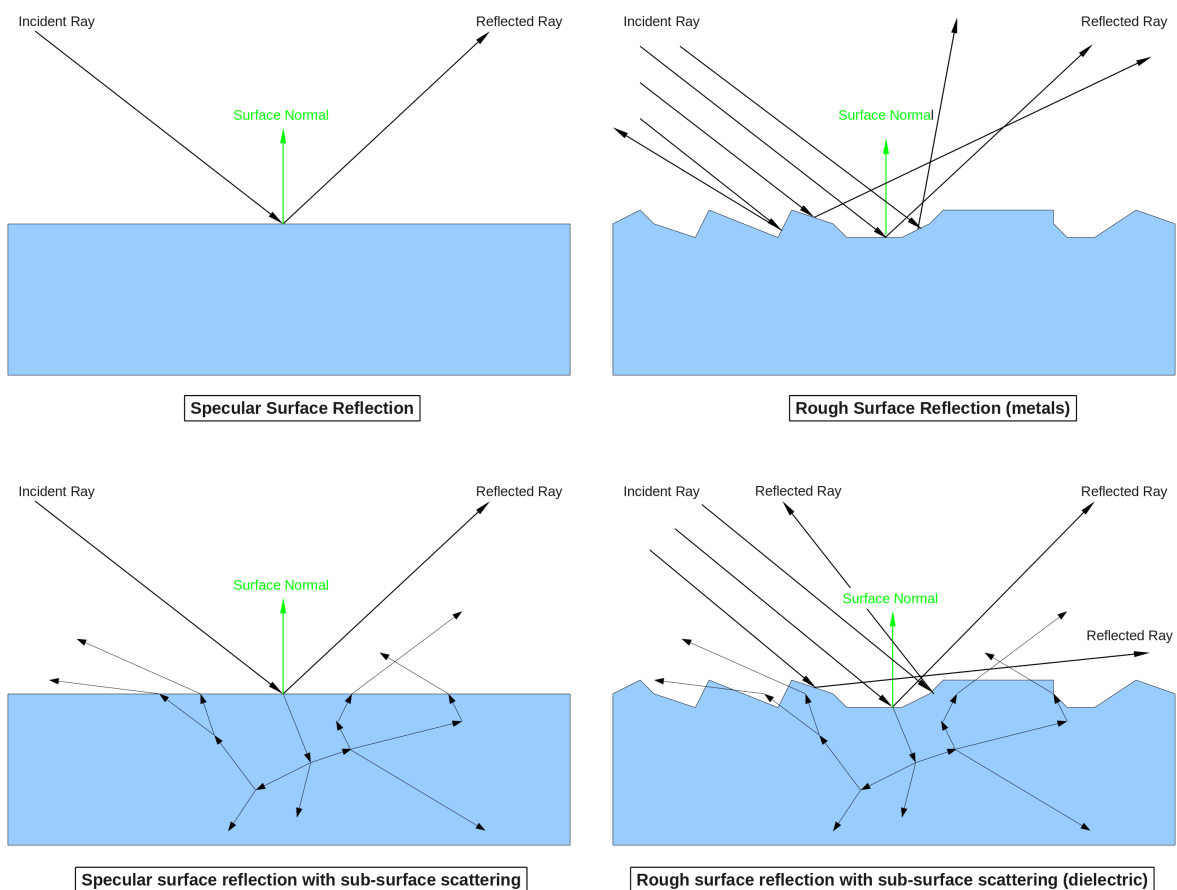

Figure 3: Surface scattering geometries used in this study.

Figure 3 shows the cases of interest for this paper. The simplest case, shown in the upper left, is specular scattering from a surface interface, such as would occur from a piece of shiny metal or a dielectric that is a volumetric absorber. The upper right case would apply for metals with rough surface finish. Keep in mind that the roughness shown here is large compared to the wavelength but small compared to the overall

surface geometry; it is due to surface finish on scales less than about a millimeter in most cases. The bottom two cases in Figure 3 are for dielectrics the exhibit volumetric (or subsurface) scattering. For our model to accurately describe solar scattering we must take into account all four scattering cases. We do this using a statistical Multi-Facet (MF) scattering approach as described in the next section. The only scattering case we have not shown if Figure 3 is the case of multiple surface scattering. Since all of the cases we will examine in this paper are at incident angles greater than 20° (phase angles > 40°), multiple surface scattering will have a negligible effect on the scattered light.

Microfacet Model

The requirements for our model are: that it be radiometrically accurate, conserve energy, exhibit Helmholtz reciprocity and be numerically tractable. This last point is important since any real time application of our polarization approach will require many calculations per second.

Figure 6 shows examples of measured and computer generated images of satin tape wrapped around a spindle. The computer generated image is practically indistinguishable from the real image. This is no accident, the method used to generate the image on the right is physics based and radiometrically accurate. Figure 4 shows another image of a computer generated satin cloth draped over a table. The subtle change in hue with angle that is characteristic of satin is even reproduced. Figure 5 Shows a computer rendering of a transparent globe with rough (frosted) surface features. The images in Figures 6-5 were generated from first principles using a Micro-Facet (MF) based model of light scattering. The overall geometry were modeled using standard computer graphics methods.

The MF approach grew out of a desire by the computer gaming and movie animators for more realistic scene generation. In this approach, effects due to the surface structure on scales smaller than a wavelength can be ignored. This assumption has been shown by rigorous calculations to be appropriate[18] since, any diffraction effects will average out at normal viewing distances. Surface geometry at scales much greater than the surface roughness correlation distance are modeled explicitly using standard 3-D modeling methods such as: polygonal (macro) facets, geometric primitives or Bezier splines. The meso-scale, between the microscopic diffraction scale and the explicitly described macro scale, included all of the "surface roughness" scales and are modeled statistically. In this approach the surface is modeled as an ensemble of microfacets (Figure 7). These facets need not be planar; they can have any number of geometric and physical properties. However, Ashikhmin[12] and He[18] have shown that triangular, plainer facets are sufficient to describe any surface; in fact, in the limit that the size of the micro-facets goes to zero, all of the facets can be identical in shape. In the case of identical, planar microfacets, only three parameters are necessary to fully describe the surface micro-structure: the distribution of surface normal directions, the surface roughness and the material index of refraction.

Figure 4: Computer rendering of velvet

Figure 5: Computer rendering of transparent globe.
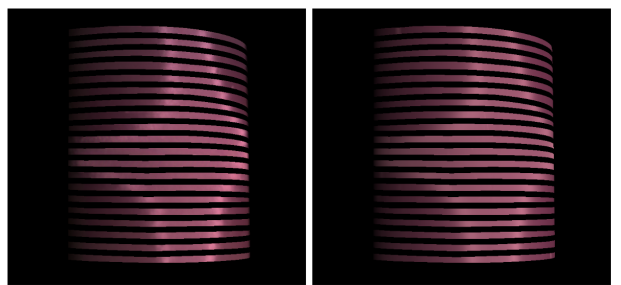
Figure 6: Left: Real image of purple satin, Right: Computer generated image[1]

We have chosen to use a the Blinn-Phong normal distribution to describe the microfacet normal distribution

$$\rho(h) = \left(\frac{m+1}{2\pi}\right) cos(\hat{h} \cdot \hat{n})^m \tag{11}$$

Here, $\hat{h}$ is the microfacet normal, $\hat{n}$ is the local average (macro-scale) surface normal and m is a surface roughness parameter proportional to the inverse of the surface correlation distance. A Lambertian surface would have $m = 0$ and a mirror surface would have $m = \infty$. This distribution has a number of computational advantages and, more importantly, it has been experimentally justified[11] for a number of materials. While the results presented here use the Blinn-Phong normal, there are no a priori restrictions on the distribution, it is not even required to be analytic.
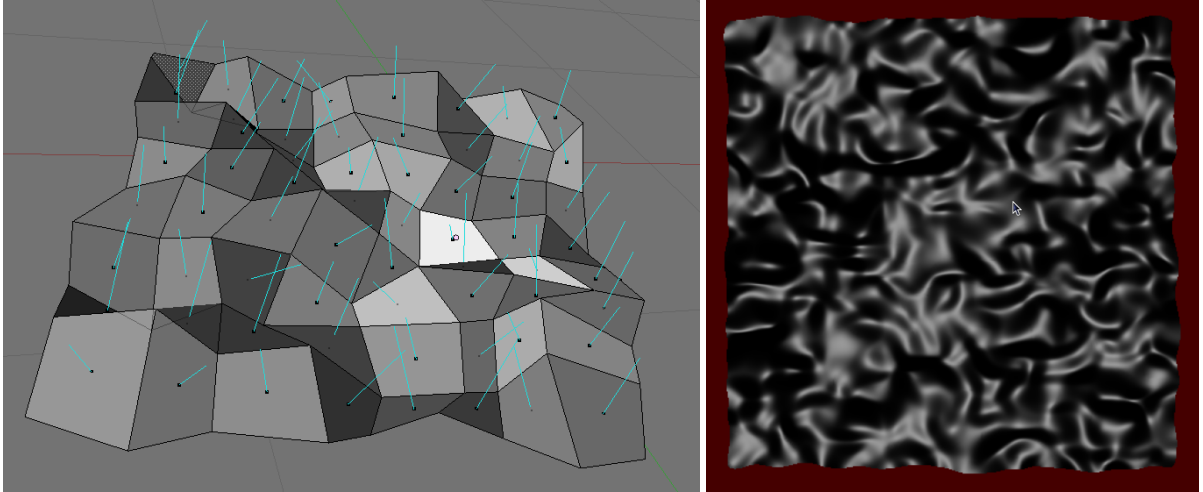
Figure 7: Left: microfacet surface, blue arrows are normals. Right: fractal surface with 130k facets

One of the key features of the microfacet theory is the concept of microscopic shadowing and masking (Figure 8). If under illumination a microfacet is shadowed by another microfacet it does not contribute to the BRDF. Likewise if a microfacet is not visible to the "viewer" then it is said to be masked, and does not contribute to the BRDF. Since, the BRDF is symmetric with respect to interchange of k and k' we will henceforth refer to both effects as shadowing. Thus, the microfacet BRDF can be written as:

$$f(\hat{k};\hat{k}') = \left(\frac{\rho(\hat{h})}{<\hat{n}\cdot\hat{h}>\left(\hat{n}\cdot\hat{k}\right)} \right) F(\hat{k},\hat{k}')P(\hat{k}|k') \tag{12}$$

Here the factor $P(k|k')$ if the probability that a microfacet is visible from both the k and k' directions and contains the shadowing effects. The term $F(k|k')$ is the Fresnel refection term which contains the surface physics. In his original work, Ashikhmin used the unpolarized (average) Fresnel approximation of Shick[6]:

$$F(k;k') = F_0 + (1-F_0)\left(1-\left(\hat{h}\cdot\hat{k}\right)\right) \tag{13}$$

Figure 8: Shadowing and Masking

Here $\hat{h}$ is the half-angle vector between k and k', which is just the microfacet normal, and F_0 is the Fresnel reflection factor for normal incident angle. The term $<\hat{n}\cdot\hat{h}>$ in Equation 12 is the ensemble average over the distribution $\rho(\hat{h})$.

Ashikhmin et al. have shown that the general form of the shadowing term, $P(k|k')$ in Equation 12 is:

$$P(k|k') = (1-f(\phi))\,P(k)P(k') + f(\phi)min\,(P(k),P(k')) \tag{14}$$

where $f(\phi)$ is a function of the angle, ϕ, which is the angle between the projections k and k' onto the plane normal to $\hat{n}$, the surface normal. For our work we choose the simplest form for $f(\phi)$ which is consistent with Equation 14 namely, $f(\phi) = cos(\phi/2)$. Finally, the function $P(k)$ is the probability that a microfacet is visible from the direction k:

$$P(k) = \frac{<\hat{n}\cdot\hat{h}>\left(\hat{n}\cdot\hat{k}\right)}{<\hat{h}\cdot\hat{k}>_+} \tag{15}$$

Here the ensemble average, $<\hat{h}\cdot\hat{k}>_+$, is over all microfacets that are not shadowed (or masked). For details on the derivation refer to Ashikhmin's paper[2]. The important point here is that once the microfacet normal distribution is specified, the BRDF is specified. Also note that this BRDF only contains contributions from single bounce (specular) reflections, To account for multiple reflections, Ashikhmin et al enforced energy conservations and reciprocity to derive a unique expression for the multiple reflections (diffuse) reflection term.

$$f_d = c\,(1-R(k))\,(1-R(k')) \tag{16}$$

Here the function $R(k)$ is the total hemispherical specular reflectance for light incident from direction k. The total BRDF is then the sum of a specular (single reflection) and a diffuse (multiple reflection) BRDF:
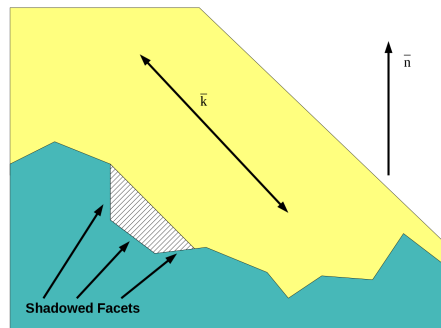
$$f = f_{specular} + f_{diffuse} \tag{17}$$

The optical effects that this simple, physics based approach is capable of reproducing is quite striking (Figures 6,4). For non-normal illumination, multiple reflections depolarize, and the diffuse term gives the depolarization. Thus, if depolarization is the only polarimetric quantity of interest this formulation is a good approximation. Though not shown here, the Ashikhmin-Shirley approach can also represent simple surface roughness anisotropy by introducing an anisotropic $\rho(h)$[12] (see Figure 9).

However, if we want to model the polarimetric quantities such as retardance, diattenuation and polarizance a more sophisticated approach is warranted.

Model Implementation

In our model we replace the simple Fresnel term of Shick (Equation 13) with a rigorous vector polarization treatment. We also include terms for subsurface scattering for dielectrics and treat the polarized and unpolarized light separately. For the polarized light we calculate using the scattered fields and for the unpolarized light we calculate using the scattered intensity. We include wavelength dependence of the index of refraction and of the subsurface scattering and absorption.

Figure 9: Anisotropic silk, from Kautz et al[4]

Our computer implementation draws upon the experience of the real-time computer gaming industry, namely the use of specialized graphics hardware. Until recently, complicated illumination calculations like ours would require hours on a computer using ray-tracing techniques. However, recent hardware implementations using Graphical Processing Units (GPUs) such as NVIDIA™8000 and 9000 series graphics boards has made it possible to render (generate) thousands of full 3D realizations per second. This hardware is available for only a few hundred dollars and is available for almost all computing platforms. In addition to the NVIDIA™GPU hardware, we make use of a number of software programming tools including: OpenGL, a 3D graphics package; GLSL, the OpenGL Shader Programming Language and CUDA, NVIDIA's general purpose computing language for GPUs.

One of the implementation choices we made was to use a shader based rendering approach rather than a ray tracing approach. The details of this trade-off are beyond the scope of this paper. While ray tracing is a more general approach, for most applications, the shader approach is best because of the tremendous increase in speed. Figure 10 shows some results from Kautz[4] et al that compare the ray tracing to the shader approach for rendering cloth using BRDFs.
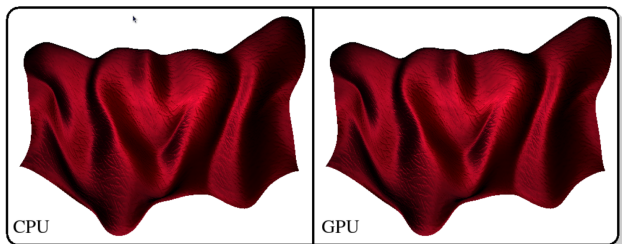

Figure 10: Left: ray traced image; Right, shader generated (from [4])

Polarization and Scattering

To handle general polarization effects in a rigorous manner is simply a matter of replacing the unpolarized Fresnel term of Shick[6] with the full Fresnel representations for the s and p polarizations:

$$r_s = \frac{\sqrt{n^2 - sin(\theta)^2} - cos(\theta)}{\sqrt{n^2 - sin(\theta)^2} + cos(\theta)} \tag{18}$$

$$r_p = \frac{n^2 cos(\theta) - \sqrt{n^2 - sin(\theta)^2}}{n^2 cos(\theta) + \sqrt{n^2 - sin(\theta)^2}} \tag{19}$$

-

Here n is the index of refraction of the material and θ is the angle of reflection with respect to the *microfacet* normal. Note, that the above Fresnel equations, *for the reflection field amplitudes,* are valid for complex n and thus can be used with metals or dielectrics. By adding the polarization in this way we can now calculate polarimetric quantities such as: retardance, diattenuation and depolarization

On interesting observation about the MF approach is that at the microscopic level all (microscopic) single bounce reflections are specular, independent of the scattering angle. In a previous paper we showed that except for near normal incidence above, multiple surface scattering has a negligible effect [16]. The MF description of all scattering as specular single scattering might at first thought seem wrong however, experimental studies by Ngan et al[14] have validated that MF approach for a large variety of surface materials, finishes and geometries. Figure 11 shows two photographs of a complex surface (tile floor) under large incident-angle illumination. The image on the left is under natural sunlight; the image on the right is under the same lighting conditions but with a polarizer that rejected the S-polarization. Two effect are evident here: one, the majority of large angle scattering is due to a single polarization (Brewster angle effect) and

two, the scattered S-polarized light is nearly achromatic. In the left image, the color is washed out due to the specular scattering whereas, in the right hand image, the low angle of incidence scattering of ambient room light leads to deeper hues. In most materials the color is determined by selective absorption during subsurface scattering (see Figure 3). In the left image the reflected light is dominated by single scattering from the surface.

Figure 11: Left, unpolarized light image. Right, P-polarization blocked with polarizer

For metal such as gold or copper, the chromatics dispersion occurs because of the variation of the index of refraction with wavelength not because of subsurface scattering. This is illustrated in Figure 12where the index of refraction for gold (Au) is plotted versus wavelength. Interestingly, for surface scattering at large angles, reflectivity approaches unity *independent* of the index of refraction and both conductors and dielectrics will experience more achromatic scattering (see Figure 1).

While color effects may be due to both surface and sub-surface scattering, generally only surface reflections cause in polarization effects. Additionally, with rough surfaces there may also be chromatic effects from surface reflections due to the apparent surface roughness effect, where the surface will "appear" to be smoother to longer wavelengths. this effect is intensified for large scattering angles. Whereas this effect may produce a strong intensity modulation, it leaves the polarization unaffected. This effect is illustrated in Figure 13 where the ratio of scattered intensity between the blue and red light (425nm/650nm) is plotted for three different surface roughness of gold.
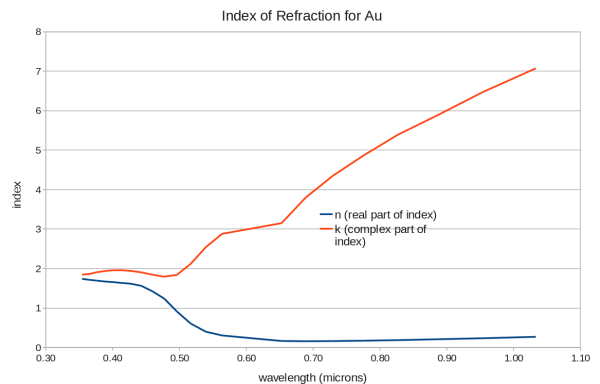
From our discussion so far it is clear that single scattering from the surface of material will dominate its polarization signature at large incident angles. For this paper we will restrict ourselves to geometries where the scattering angle is greater than 25° so that we may ignore multiple surface scattering. Without double scattering it is not possible to generate circular polarization from unpolarized light. Additionally, only a few materials are known to produce circular polarization from subsurface scattering; one such example is Scarab Beetle wings. To this end, we will only investigate the diattenuation effects, or more precisely the linear polarizance. Finally, with our parametrization of the Stokes Vector (Figure 4) the Mueller matrix reduces to:

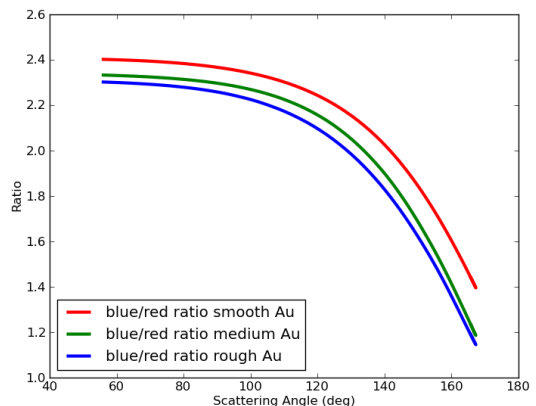Figure 12: Dispersion in the index of refraction of gold.

Figure 13: Chromatic effects of surface roughness.

$$\begin{bmatrix} S'_0 \\ S'_1 \\ 0 \\ 0 \end{bmatrix} = \begin{bmatrix} M_{00} & 0 & 0 & 0 \\ M_{10} & 0 & 0 & 0 \\ 0 & 0 & 0 & 0 \\ 0 & 0 & 0 & 0 \end{bmatrix} \cdot \begin{bmatrix} S_0 \\ 0 \\ 0 \\ 0 \end{bmatrix} \quad (20)$$

Where, M_{10} is a measure of the ability of a material to produce linear polarization for unpolarized light. For the remainder of this paper we will refer to the normalized quantity:

$$Q = \frac{M_{10}}{M_{00}} = \frac{S'_1}{S'_0} \quad (21)$$

as the Diattenuation Coefficient. Here we have chosen the letter Q to remind us that the material is producing a non-zero diattenuation, $S = Q$.

Material	425nm			550nm			650nm		
	n	k	R_{sub}	n	k	R_{sub}	n	k	R_{sub}
Au	1.62	1.94	0	0.359	2.69	0	0.170	3.14	0
Al	0.556	5.146	0	1.015	6.627	0	1.558	7.712	0
BK7 (glass)	1.527	0	0	1.518	0	0	1.514	0	0
Si (Amorphous)	5.15	0	0.1	4.77	0	0.1	4.46	0	0.1
Spectralon (PTFE)	1	0	1	1	0	1	1	0	1
Mylar (copper color)	1.10	0	0	1.5	0	0	1.6	0	0

Table 1: Materials used in this study

Results

We examine the polarization signatures from two specific types of space objects: Satellites in Low Earth Orbit (LEO) and space debris. The orbital dynamic are calculated using SGP-4 Two Line Elements (TLEs). Sun location and Earth rotation are all calculated and compared in Earth Fixed Geodetic coordinates. Sun occultation by the Earth (termination) is accounted for and only sunlit geometries are considered. Figure 14 show typical trajectories for series of LEO satellite (Explorer 27) passes. The left plot shows the trajectory in azimuth and elevation tracker coordinates and the right plot shows the phase (sun-observer) angle as a function of time since illumination began.
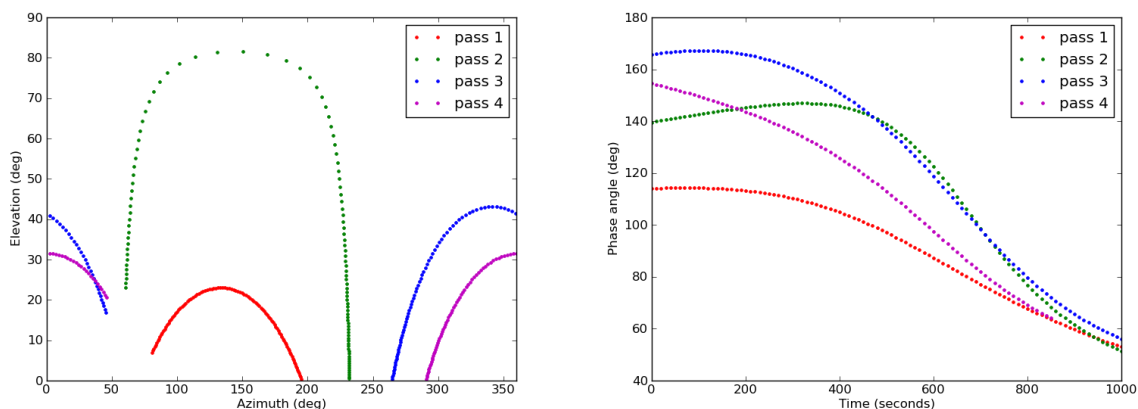

Figure 14: 8 consecutive passes of Explorer 27. Left is in tracker Az-El space and on right is phase angle versus time

We will consider the polarization effects at three different wavelengths: blue (425nm), green (550nm) and red (650nm). The actual band passes are shown in Figure 15. The choice of wavebands is not critical, we could easily have chosen Johnson UBVRI filters. However, we chose the RGB filters because all three fit within the bandpass of most Si based ccd cameras. Also, if the method described here works for such closely spaced wavelengths it should will work even better for more widely spaced bands such as the Johnson UBVRI bands used by astronomers.

The simulations were run for a number of materials; Table 1 list the materials and the corresponding material properties used. It is important to remember that these properties, while reasonable may be different that actual materials that have experienced a prolonged space environment. The goal here was to demonstrate the feasibility of our approach by using a variety of representative materials. The first 2 materials int Table 1 are metals, BK7 is a transparent glass, amorphous silicone is a high index material, Spectralon™is a very lambertian (non-polarizing) volumetric scatterer and Mylar™is a specular plastic.

The first test we ran was to look at the linear diattenuation coefficient,Q ,as a function of the three wavebands (RGB) defined above. Figure 16 shows

Figure 15: The RGB band passes used in this paper

Q as a function of phase angle and waveband for the six materials above. From a discrimination point of view these results are very good news. The BK7 and Mylar are similar for Q but, since BK7 is transparent, they can easily be discriminated from each other using total reflectivity. While the behavior in Figure 16 is nice, real space objects have complex shapes.

One of the predictions of MF theory is that for objects composed of a single material, the Q signature will be independent of shape and orientation. To verify this we used 2 shapes (Figure 17): a chamfered cube and a cigar shape. The chamfered cube provides an object with specular facets while the cigar shape has no facets.
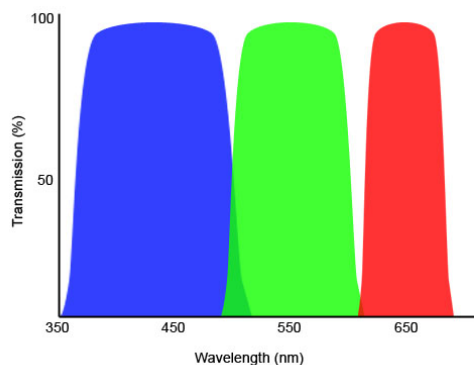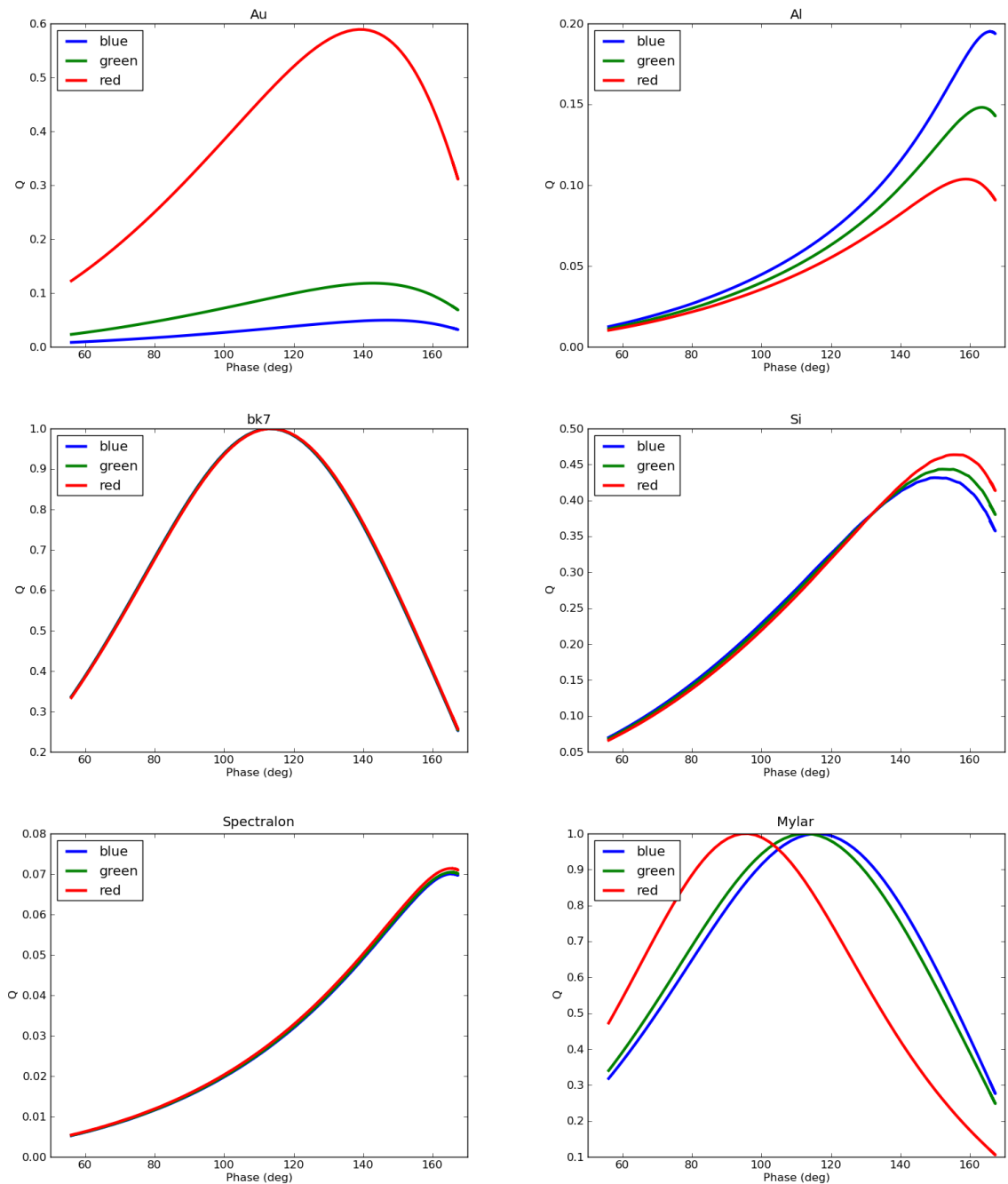
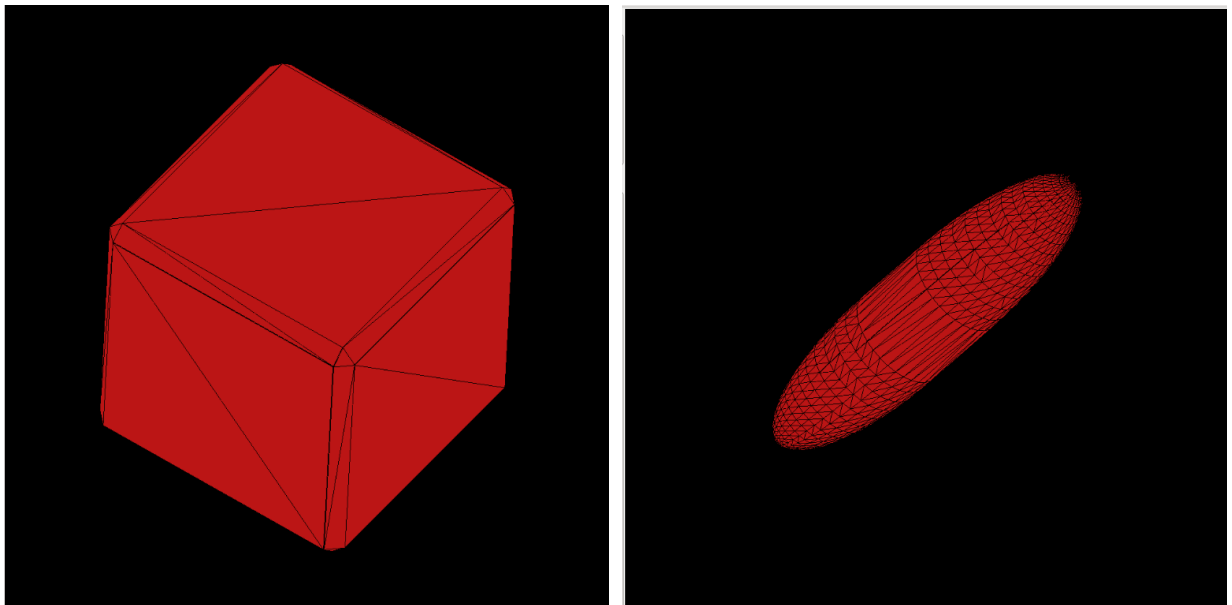Figure 16: 3 color Q versus phase angle for each material.

Figure 17: Chamfered cube and cigar shape meshes

Figure 18 shows the Q values at the three colors (RGB) for 100 random poses for two shapes and two materials (Au and Al). The plots for the chamfered cube is noisy because of the low number of body facets leads to noise in the surface normal calculation. This noise is not present in the cigar shape because it has a sufficient facet count. It is clear from Figure 18 that for single material objects, the 3-color Q signature is independent of shape and pose. Also, note that for all of the plots in Figure 18 the Sun phase angle was 140°; however, changing the phase angle may change the Q values but if will not produce a dependence on pose or shape.
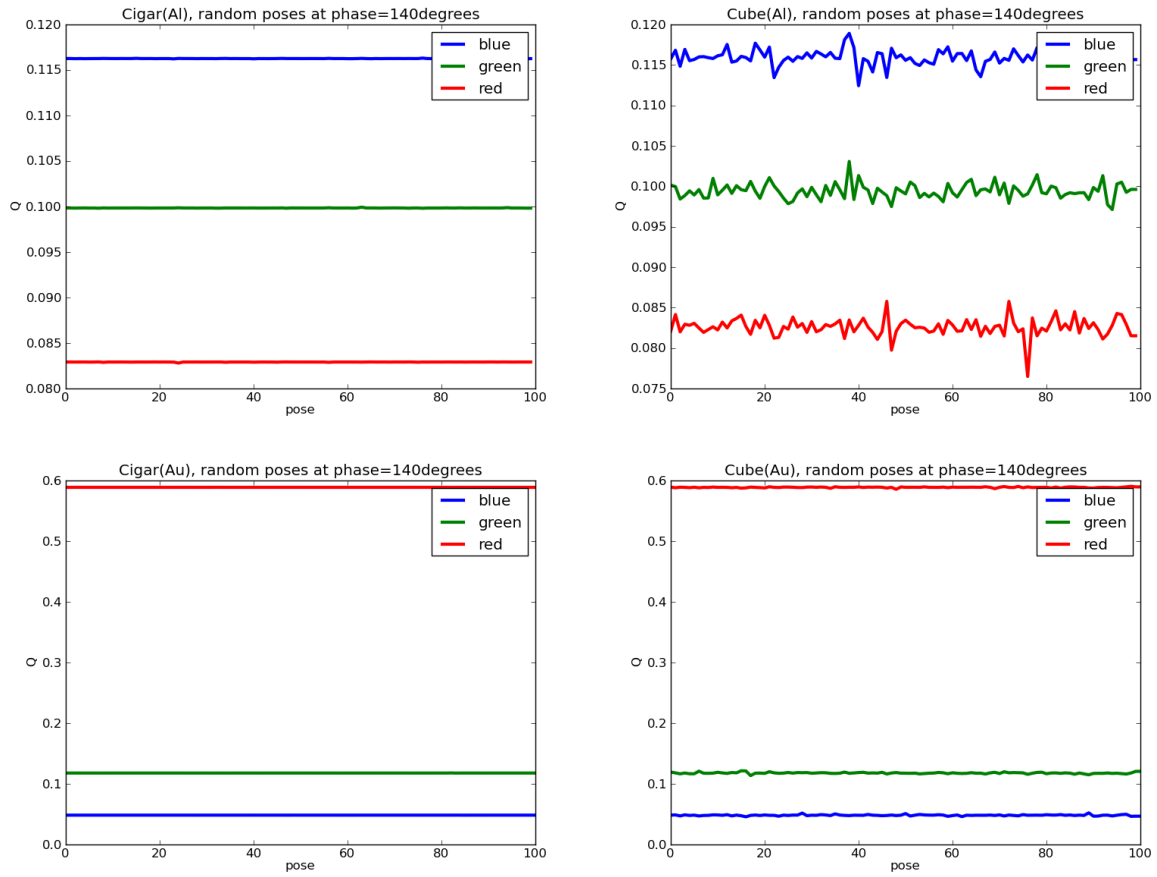
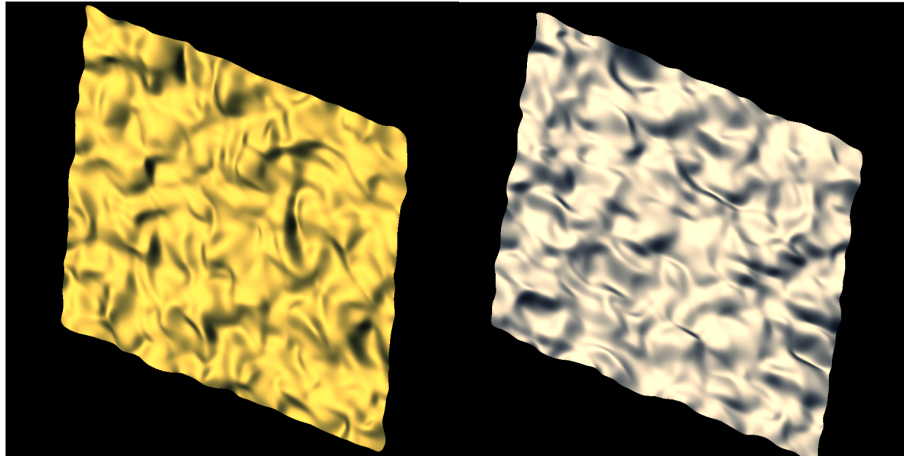Figure 18: Q values for 1000 poses of Cube and Cigar for both Au and Al

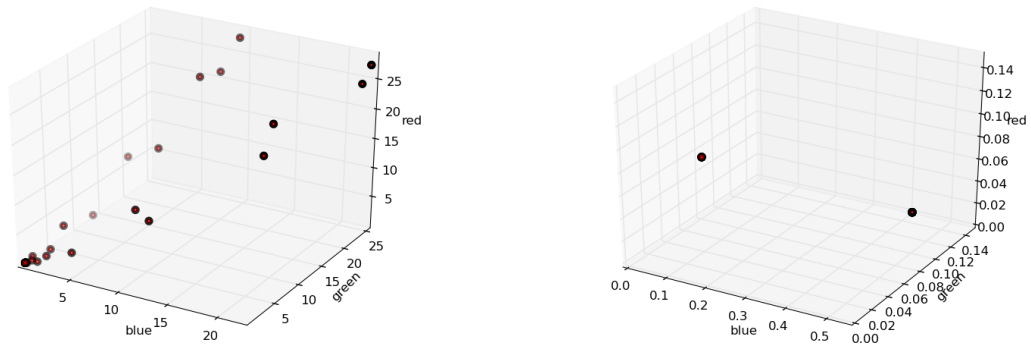Figure 19: Au/Al MLI model used in this study

Figure 20: Tumbling MLI in I-RGB (left) and Q-RGB (right) space.

Now consider a more complicated material such as a piece of multi-layer insulation (MLI). In Figure 19 we show a simple model of MLI where one side has a metallic gold coating and the other has an aluminum coating. As this object tumbles we would expect the polarization signature to simply modulate back and forth between the value for gold and aluminum. The right hand plot in Figure 20 shows the results of using the three Q values for the debris as the components in a $(Q_{red}, Q_{green}, Q_{blue})$ vector space. In this Q-RGB vector space (for a fixed solar phase angle) a given material corresponds to a specific point. If a piece of debris is at GEO, then for short periods we can consider the solar angle to be constant and the Q signature of a tumbling piece of MLI, like the piece modeled above, will just oscillate back and forth between two points in Q-RGB space, one for Au and one for Al. This is precisely what our model predicts as seen in the right hand plot in Figure 20where, the point on the left is for gold and the one on the right is for aluminum.

On the left hand side of Figure 20is the corresponding RGB Intensity (I-RGB) space plot. Clearly, in the I-RGB plot the signature is much more complicated.

For the next exercise, we looked two more realistic shapes: an Agena rocket body and the Hubble Space Telescope (Figure21). Remember that only the 6 materials from Table 1 were used for the two models. I was not our intent to produce exact rendering of the HST and Agena object, we only wanted to achieve reasonable amount of realism while providing test objects for this paper.
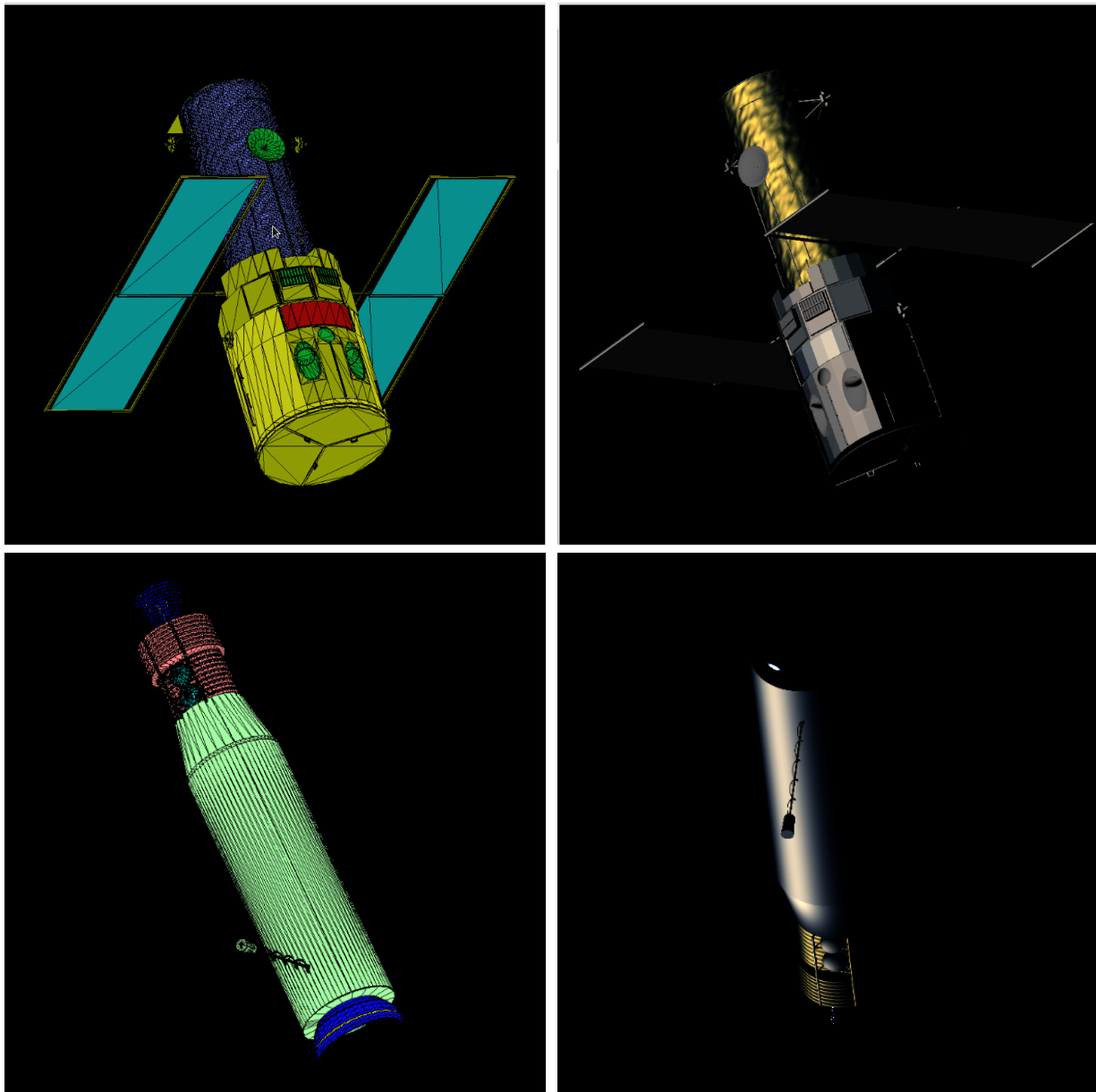

Figure 21: HST and Agena shapes. Mesh (left) and sample rendering (right).

Now that we have higher fidelity object models we can look at some more realistic LEO scenarios. Figure 22 shows the total scattered intensity, I, and the diattenuation factor Q for a single pass of the Agena and HST objects. The Agena results are on top and the HST results on the bottom and all graphs are plotted against the phase angle. The three colors represent the three RGB wavebands discussed earlier.

The first thing to note is that the I and Q plots have different shapes and they even appear to be complementary; when the I plot shows little spectral variance the Q plot shows significant variance and conversely, when the Q plot shows little spectral variance the I plot shows significant variance. This illustrates what we expect to see namely, that the polarization signature provides additional information about the object not contained in the intensity.

Our original hypothesis was that the polarization signature would help us discriminate objects. Whereas with simple shapes the polarization signature was shape independent (Figure 18), we do not expect that to be true for asymmetric objects composed of multiple materials. For those complex shapes the mixture of material "seen" by the observer will depend strongly on the pose (see Figure 21). To understand this better we plotted the polarization signatures of the Agena and HST objects for 1000 random poses each at three different solar phase angles.

Figure 23 shows this data plotted in Q-RGB space. The top row is fora phase angle of 60° the middle row is for 100° and the bottom row is for phase angle 140°. The three horizontal plots show three different perspective views of the same data. The blue data is 1000 random poses of the HST target and the red data is 1000 random poses of the Agena rocket body. Two effects are immediately evident; first, the HST and Agena data *does not* overlap in Q-RGB space and second both the Agena and HST data appear to lie on planar 2D surfaces.

The fact that the Agena and HST data don't overlap in Q-RGB space is probably just luck, though a further investigation with more shapes is warranted. The fact that both the HST and Agena data are restricted to 2D surfaces in Q-RGB space is more interesting. While some of the data points fo HST lie off the plane,
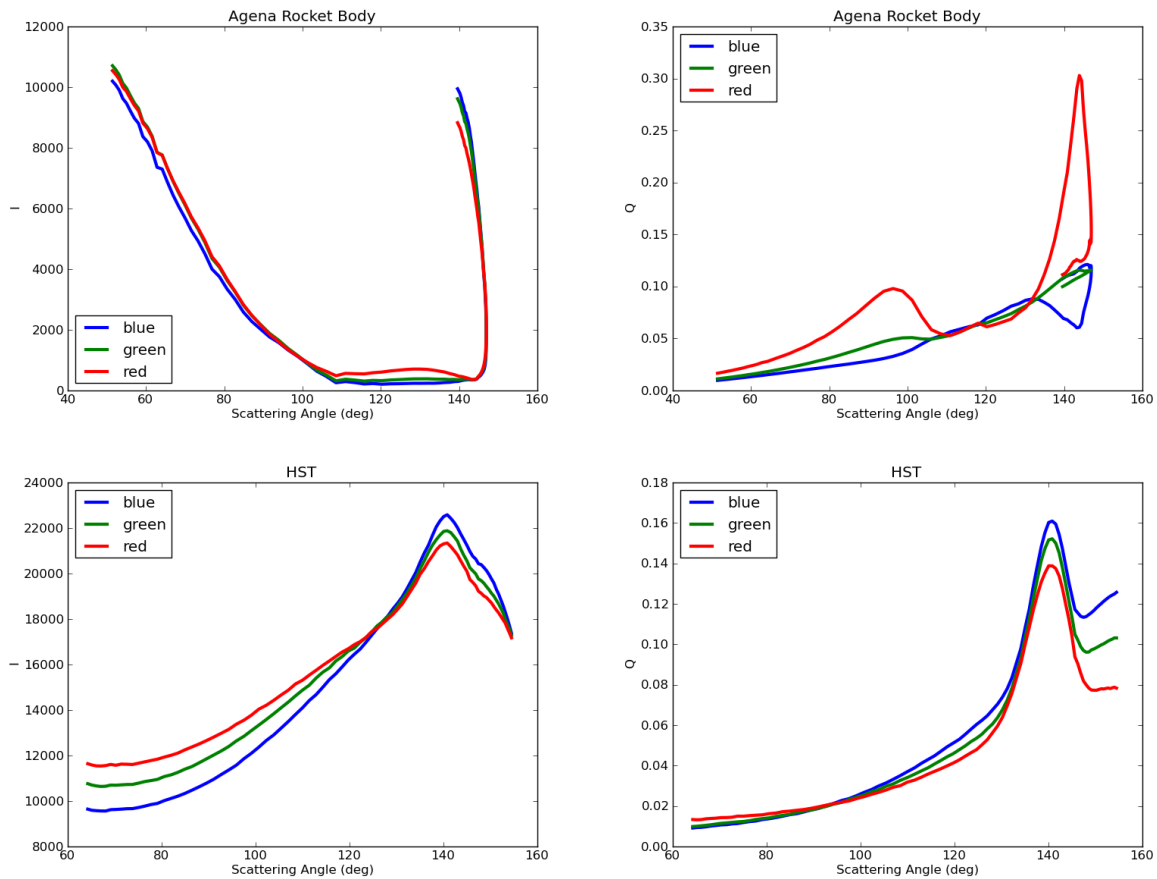
Figure 22: Agena and HST single pass results: Intensity (left) and Diattenuation (right).

they appear to come from poses with very low SNR and as such can be ignored. The co-planarity of the data for a given shape may be explained by the fact that the Q's for a given material have a fixed relationship independent of pose, for a given phase angle, (Figure 18). If the phase angle is constant, then changes in poses are simply changes in ad-mixtures of material with constant Q relationships.

$$Q = c_1 Q_1 + c_2 Q_2 + c_3 Q + ... \quad (22)$$

Here the c_i are functions of pose. If we let the c_i be a function of rotations in 3 dimensions, Euler angle for instance, then we can show that only two of the rotation angle are independent and thus, Q is a 2-dimensional surface in Euler space. This can be visualized by imagining that you rotate a shape about the line of sight, in this case the ad-mixture (Q) will not change thus, Q is degenerate in rotations about the line of sight and only 2 rotations are needed to describe the admixture for Q. Now the position in Q-RGB space can be written as a vector of Qs:

$$Q_{rbg} = \begin{pmatrix} Q_r \\ Q_g \\ Q_b \end{pmatrix} \quad (23)$$

Thus Q_{rgb}, the position in Q-RGB space is only a function of two variables (2 angles) and for a given composite object all possible poses will lie on a 2-dimensional surface in Q-RGB space.

The argument we just made for the co-planarity of the points in g Q-RGB space assumed a fixed solar phase angle. From the different rows in Figure 23 it is clear that the planar surfaces change with phase angle, but very slowly. Figure 24 shows 8 consecutive passes of the HST (top) and the Agena (bottom) plotted in Q-RGB space. Once again the Q_{rgb} points are constrained to a plane. This was not expected on the basis of our argument above, where we concluded that the addition of the third degree of freedom (phase angle) should have broken the symmetry in Q-RGB space. A possible explanation for this is that the all of the satellite passes in Figure 24 had stable pointing and that over a short period of time (like a single pass) the change in the pose of the satellite can approximated by a single rotation about the center of the earth: thus, reducing the degrees of freedom back to 2 (rotation and phase angle). This is speculative and needs to be investigated more thoroughly.

Real Time Calculations

Our approach allows us to generate high fidelity polarization signatures for solar illuminated space objects in real time. This capability can enable several real time applications such as: Space object ID verification, satellite aging and health monitoring and real time pose and material estimation for unresolved satellites. With the microfacet and GPU approach it is possible to generate signatures "faster that real time" so we can search the Q-RGB parameter space for real time classification and ID. If the apparent 2D co-planarity symmetry in Q-RGB space turns out to be correct then, classification and ID tasks will be greatly accelerated.
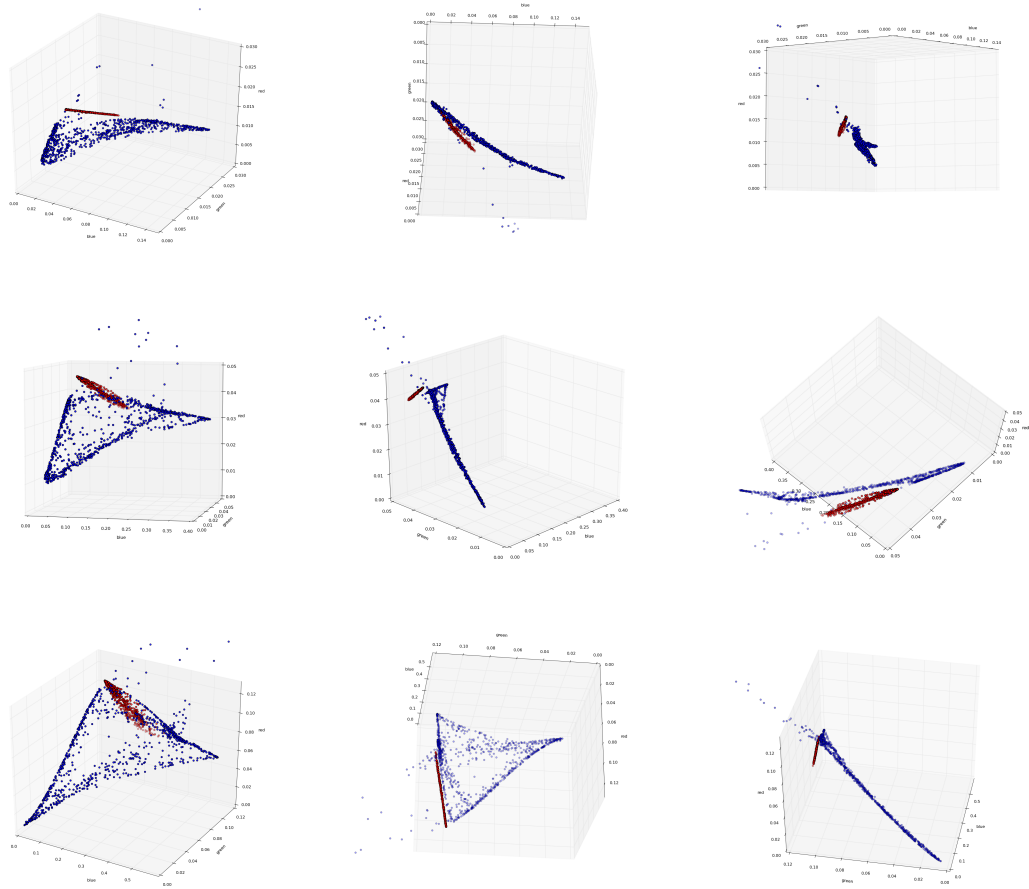
Figure 23: Q-RGB space graphs for 1000 random poses of HST (blue) and Agena (red). Top row is for phase angle of 60°, the middle row is for 100° and the bottom is for 140°. Within a row are three view of the same data.
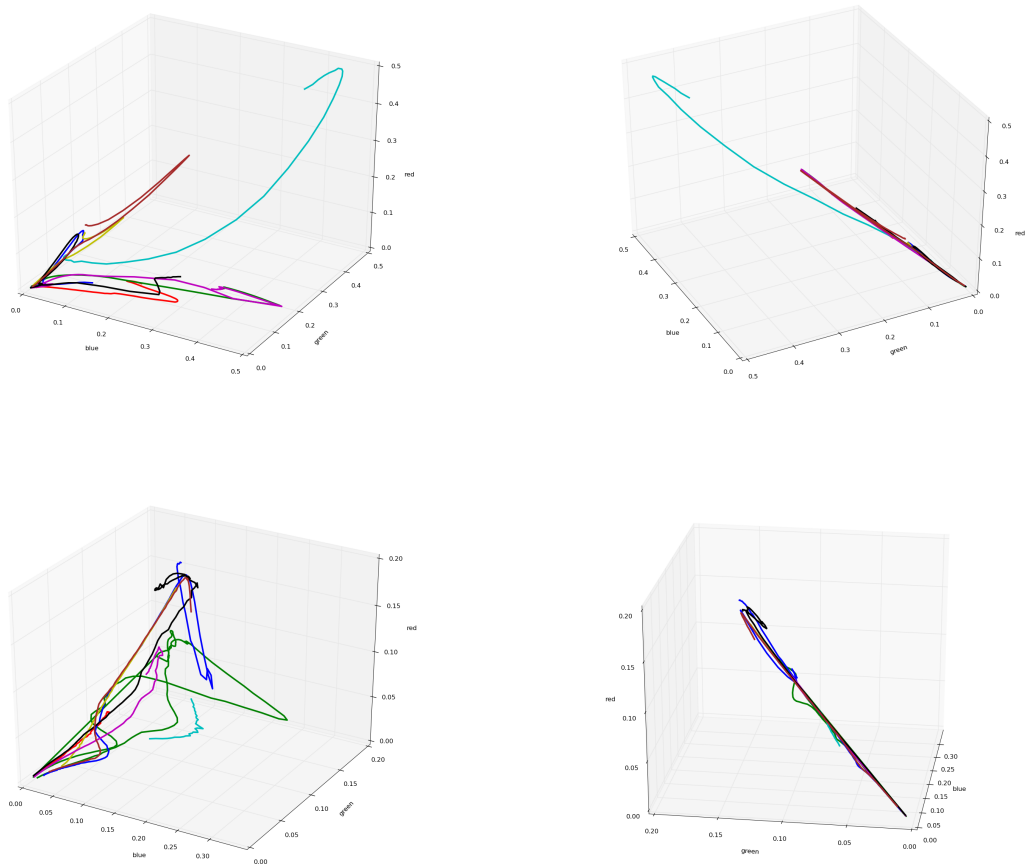

Figure 24: Trajectories in Q-RGB space for HST (top) and Agena (bottom). Within a row are two view of the same data.

Summary

We have developed polarization extensions to the Ashikhmin's microfacet scattering theory. These extensions are physically based and yield BRDFs that conserve energy and Helmholtz reciprocity. This approach allows us to accurately describe the physics of polarized for light scatter from complicated objects. This includes effects such as shape, orientation, material and surface finish. The microfacet approach is very general and can be easily extended to handle multilayer surfaces, emission, and refraction and transmission. Even complicated, textured material like cloth, scratched metal and wood are readily modeled. With minor modifications our approach can also handle reflections from liquids, gasses and particulates[1, 5]. Also, our GPU implementation will allow use to extend the current code to include thermal emission effects and atmospheric effects like turbulence and transmission). The computational speed of our MF scattering model could enable a host of real time applications including: space object ID verification, satellite aging and health monitoring, and real time pose and material estimation for unresolved satellites

We also presented a framework for discussing polarization effect in satellite "light curves" and discovered a potentially valuable symmetry for material diattenuation coefficients. Results of simulations show that this symmetry may greatly simplify the construction of polarization based classifiers, possibly improving real time target ID, pose and material estimation for resolved and unresolved space objects.

References

[1] Gerligand, P., Smith, M., Chipman, R. *Polarimetric Images of a Cone*, Optics Express, vol. 4, No 10, 420-430, 1991

[2] Ashikhmin, M., Premoze, S., Shirley, P., *A Microfacet-based BRDF Generator*, SIGGRAPH, 65-74, 2000

[3] Wlater et al, *Microfacet Models for Refraction through Rough Surfaces*, Eurographics Symposium on Rendering, 2007

[4] Kautz, Jan etal, *User Defined Shading Models for VR Applications*, 2005

[5] Cook R. and Torrence K., A *Reflection Model for Computer Graphics*, SIGGRAPH, 192-198, 1981

[6] Shick, C., *An Inexpensive BRDF Model for Physically based Rendering*, Eurographics, 149-162, 1994

[7] Ward., M*easuring and Modeling Anisotropic Reflection*, SIGGRAPH, 265-272, 1992

[8] He. X.D. et al, *Comprehensive Model for Light Reflection*, SIGGRAPH, 176-186, 1991

[9] Torrence, K.E. and Sparrow, E.M., *Theory of Off-specular Reflection from Rough Surfaces*, JOSA, 57, 1957

[10] Weidlich, A. and Wilkie, A., *Arbitrarily layered micro-facet surfaces*, 2006

[11] Ngan, A et al, *Experimental Analysis of BRDF Models,* Eurographics Symposium on Rendering, 2005

[12] Ashikhmin, M. and Shirley, P., *An Anisotropic Phong light Reflection Model, Journal of Graphics Tools*, 25-32, 2000

[13] Cowardin, et al., *An Assessment of GEO Orbital Debris Photometric Properties Derived from Laboratory-Based Measurements, AmosTech 2009*

[14] Stryjewski, J., Hand, D.,Tyler, D., Murali, S., Roggemann, M. and Peterson, N., *Microfacet Scattering Model for Pulse Polarization Ranging,* AmosTech 2009

[15] Fulcoly, D.m Optimizing site locations for determining shape from photometric light curves, AmosTech 2009

[16] Moriba, K., Satellite Characterization: Angles and Light Curve Data Fusion for Spacecraft State and Parameter Estimation, AmosTech 2009

[17] Klem, B., Space Object Radiometric Modeling for Hardbody Optical Signature Database Generation, AmosTech 2009

[18] Knox, K., Photomery of rotation regular n-sided prisms for arbitrary solor phase angles, AmosTech 2009

[19] Kurosaki, H.m Observations fo Light Curves of Space Objects, AmosTech 2009

[20] Rodriquez, H., Using Light Curves to Characterize the Size and Shape of Pseudo-Debris, AmosTech 2009

[22] A Comparison of Four BRDF Models Stephen H. Westin, Hongsong Li, and Kenneth E. Torrance Cornell University Program of Computer Graphics